Mechanism of negative membrane curvature generation by the IRSP53 I-BAR domain

Binod Nepal[1], Aliasghar Sepehri[1], Themis Lazaridis[1,2*]

[1]Department of Chemistry, City College of New York, New York, NY 10031

[2]Graduate Programs in Chemistry, Biochemistry, and Physics, The Graduate Center,

City University of New York, New York, New York

* Corresponding author, email: tlazaridis@ccny.cuny.edu

Keywords

I-BAR, lipid bilayer, membrane curvature sensing and generation, computer simulation.

Author Contributions

BN performed the bulk of the computations. AS contributed in the construction of the oligomers. BN and TL designed the research and wrote the manuscript.

Abstract

The membrane sculpting ability of BAR domains has been attributed to the intrinsic curvature of their banana-shaped dimeric structure. However, there is often a mismatch between this intrinsic curvature and the diameter of the membrane tubules generated. For example, I-BAR domains are almost flat but generate much higher membrane curvature. Furthermore, F-BAR and I-BAR domains are quite similar, but the former generates positive curvature and the latter negative curvature. Here, we use implicit-solvent computer modeling to show that the membrane bending of the IRSP53 I-BAR domain is dictated by its oligomeric structure, whose curvature is completely unrelated to the intrinsic curvature of the dimer. We find that I-BAR dimers undergo lateral and end-to-end interactions to form higher oligomers. The lateral interactions, which can occur with varying register, are stronger and give a curved shape that has the membrane binding interface on its convex surface. Two other I-BARs (MIM and I-BARa) gave similar results, whereas a flat F-BAR sheet curved to make its membrane binding interface concave, consistent with positive membrane curvature generation. Individual dimers orient parallel to the tube axis when the tube radius is small, whereas perpendicular orientation is preferred for larger diameter tubes. This orientational preference exists even in the higher oligomeric form. Helical spirals on tube interiors are stable at a density comparable to experimental measurements. The sorting ratio computed from our membrane binding energies is also consistent with experimental measurements.

Significance Statement

Changes in membrane shape are required in numerous biological processes, such as endocytosis/exocytosis, viral budding, filopodia formation, etc. The BAR domains are one protein family that mediates these changes, but their mechanism of action is not entirely clear. The BAR domains possess an intrinsic curvature but this curvature often does not match the curvature of the membranes generated.This is especially true of the I-BAR domains which are known to generate negative curvature. Here, we show that a well-studied I-BAR domain forms oligomers that possess a curvature unrelated to the intrinsic curvature of individual dimers and matches the membrane curvatures generated. This resolves a long-standing mystery about the mechanism of negative membrane curvature generation.

Main Text

Introduction

Remodeling of the cell membrane is involved in key biological processes such as endocytosis, viral budding, and membrane fission/fusion (1-8). This is usually accomplished by specialized proteins that can sense and generate membrane curvature. The mechanisms by which proteins do this have attracted intense interest. The “wedge” mechanism involves shallow insertion of an amphipathic helix on the membrane surface inducing an asymmetric stress that bends the membrane in the opposite direction (9-14). The scaffolding mechanism posits that the specific shape of certain proteins and/or their oligomers acts as a scaffold for membrane bending (15-18). Unstructured proteins and protein-protein crowding have also been proposed to cause membrane bending at high protein density (19-23).

One important class of scaffolding proteins is the BAR domain family, consisting of crescent-shaped dimers. Depending on the size and shape of the curvatures they stabilize or generate, they are classified into three groups: classical BAR/N-BAR, F-BAR, and I-BAR domains. Classical BAR/N-BAR domains generate or stabilize high, positive membrane curvature. The intrinsic radius of curvature of classical BAR dimers ranges from 12 to 40 nm (24-26) but can be as small as 5.5 nm for APPL1 (27). The N-BAR domains contain an additional N-terminal amphipathic helix (H0 helix), which can assist in membrane binding and/or curvature generation. For example, amphiphysin, nadrin and endophilin proteins contain an H0 helix. F-BAR domains tend to generate or stabilize lower positive membrane curvature than classical BAR

domains. The diameter of the tubules generated by F-BAR domains ranges from 64-113 nm in living cells (28). The third class of BAR family proteins stabilize or generate negative membrane curvature and hence are called inverse BAR or I-BAR domains. In contrast to the classical BAR domains, they have a positively charged surface that is slightly convex in the crystal structures, which is thought to help them bind efficiently on the concave surface of the membrane. I-BAR domains are present in several proteins, including insulin receptor substrate P53 (IRSp53), insulin receptor tyrosine kinase receptor (IRTKS), missing-in-metastasis (MIM) and ABBA. IRSp53 and IRTKS I-BAR domains bind to the membrane mainly through electrostatic interaction but MIM and ABBA have an additional amphipathic helix which contributes to membrane binding (29).

There is evidence that membrane tubulation or generation of global membrane curvature requires assemblies of BAR proteins. For example, Cryo-EM studies found that N-BAR domains arranged in a helical lattice around the growing tube and this lattice was stabilized by H0 helices. Similar oligomeric structures have been reported for some F-BAR domains, stabilized by both tip-to-tip and lateral interactions (28). It is possible that I-BAR proteins also arrange in a helical lattice structure during membrane tubulation but evidence for this is currently lacking. Without the detailed picture of a higher order oligomer, the membrane bending mechanism of these peptides cannot be understood clearly. The binding of these proteins to PI(4,5)P2 further complicates the mechanism, as I-BAR domains were found to cause PI(4,5)P2 clustering (30, 31). Asymmetric distribution of PI(4,5)P2 promotes the membrane curvature generation even without the peptides (32) or just with simple cations like Ca^{2+} (33).

Proteins that generate negative membrane curvature bind to the inner leaflet of tubules, and this makes them harder to study. Specialized techniques have been developed for negative curvature sensing peptides in the last five years. For example, pulling tubes from a GUV with encapsulated peptides provided a way to determine the preference of the IRSp53 I-BAR domain for ~18 nm radius (34). A lower-resolution technique using plasmonic nano wells found the curvature preference for the IRSp53 I-BAR domain to be less than 40 nm radius (35). More recently, a novel method utilized protein sorting on tubular filopodia of varying diameter. The experiments showed preferential binding to 25-nm and 19-nm radii for MIM I-BAR and IRSp53 respectively (36). The curvature sensing of both I-BARs resulted from both increased dissociation constant and increased saturation density at low curvature.

Computer simulations could provide insights but are limited by the system size and computational resources. All-atom simulations usually consider one dimer on the membrane surface for a limited amount of time (37, 38). Coarse-grained simulations can handle large systems, at the cost of lower accuracy (39, 40). Few studies have appeared on I-BAR domains. A coarse-grained molecular dynamics (MD) simulation showed the generation of negative curvature but shallower than that generated experimentally (37). Moreover, the peptide was not binding through its convex surface and, depending on the binding orientation, it also generated positive membrane curvature. Combining all-atom MD simulation and site mutation analysis showed that about 30 salt bridges are formed between I-BAR and the membrane head groups (38). Membrane deformation was explained in terms of PI(4,5)P2 lipid clustering caused by these salt bridges. Another MD simulation showed similar I-BAR mediated PI(4,5)P2 clustering on the lower leaflet and curvature generation was postulated based on lipid asymmetry (41). The most recent coarse-grained MD simulation revealed that the peptide tends to orient along the axis of the 20 nm radius tube (39). Perpendicular orientation was only preferred for the larger size tubes. This result is puzzling, considering the curvature preference for 20 nm tubes. If individual I-BAR domains do not prefer to be aligned with the curvature, then how can they sense or stabilize it?

One possible explanation is that I-BAR domains form higher oligomers that are responsible for curvature sensing and generation. If so, how does each I-BAR dimer arrange to form higher oligomers? IRSP53 I-BAR generates tubules with average diameter of about 43-nm (29). What dictates this? In the present work we sought answers to these questions using an implicit membrane model for curved membranes (42) that allows treatment of the proteins in atomistic detail. We found that individual IRSP53 I-BAR dimers are only weakly curvature sensing but higher membrane charge increase the curvature sensitivity. Furthermore, we found that I-BAR dimers undergo lateral interaction to form a higher oligomer whose curvature, orthogonal to the

intrinsic curvature of the dimer, appears to be responsible for negative curvature sensing and generation.

Results

Binding orientation, energetics and curvature sensitivity of the dimer

First, the membrane binding interface of the dimer was determined on the flat membrane surface from four simulations, each initiated from a configuration obtained by rotating the principal axis of the dimer successively by 90º. These simulations show that the dimer always binds with a well-defined interface (Fig. 1a) regardless of the initial configuration. This interface contains a large number of positively charged residues. Lysines 121, 136, 143, and 147 contribute most strongly to binding, with Lysines 18, 36, 40, 122, 142, 146, 152, 156, and Arginines 29, 114 and 128 making smaller contributions (see Table S1 in Supporting Information). Consistent with previous all-atom and coarse-grained simulations (37, 38), the positively charged residues near the end regions of the dimer interact strongly whereas those in the middle region interact weakly with the flat membrane surface (Fig. 1a). Surprisingly, due to the middle region, the binding interface in Fig. 1a appears not convex but concave. The dimer binds similarly onto the interior of a 30-nm spherical membrane (Fig. 1b). The same positively charged residues contribute to membrane binding but the fit appears improved. Consistent with mutation studies (38), the middle region residues LYS 18, LYS 36, LYS 40 and ARG 29 bind less strongly than those on the arms. In the binding configuration of the dimer on the exterior 30-nm spherical surface (Fig. 1c) the middle region positive residues bind somewhat better, but there is significant loss of interactions in the arms. It seems that what matters for curvature sensing is not the curvature of the entire surface but only that of the two arms alone. The angle between the two arms, depicted in Fig. 1b, is ~154º in the crystal structure and is flatter on the flat membrane compared to the interior of the spherical surface (see Fig. S1).

The orientational preference of the I-BAR dimer on cylindrical membrane tubes is presented in Table 1. The starting orientations were either parallel or perpendicular to the tube axis. In narrow tubes, inside or outside, the dimer tends to orient parallel to the tube axis, in agreement with recent coarse-grained simulations (51). On the larger tubes this orientational preference persists only for the tube exterior. This is an indication that I-BAR dislikes a convex surface. The binding energies of the IRSP53 I-BAR dimer on 30% anionic spherical and cylindrical membrane surfaces are shown in Table 2. Binding energies on the interior spherical surface and on both cylindrical surfaces do not change much with curvature (the difference is within 0.3 kcal/mol). The latter is due to the preferred parallel orientation of the dimer to the tube axis. Only the exterior spherical surface is clearly less favorable at high curvature. Comparing the interior cylindrical and spherical surfaces, the cylindrical surface is slightly preferred, especially at higher curvature.

The curvature sensitivities of the dimer were also determined at different anionic fractions (Table 3). Binding energy is maximal at 20 nm radius (except at 30% anionic fraction) and minimal on the flat surface. At 30% anionic fraction, there is only a slight distinction between high curvature and the flat membrane surface. However, at 50 % and 75% anionic fraction this distinction increases significantly to as much as 1 kcal/mol. The curvature sensitivity parameter α (last column of Table 3), determined from the data for radii 20 nm to 50 nm, increases significantly on increasing anionic fraction. The ratio of the dissociation constants for 20 nm radius to flat membrane increases from 1 to 3 to 6 on moving from anionic fraction 30% to 50% to 75 %. Since I-BAR dimers align with the tube axis, the observed curvature sensitivity is attributed to the stronger electrostatic interaction in the narrow-sized tubes. The sorting ratio between the planar membrane and the 20-nm radius tubular membrane (Table S3) is 1.8 at 30% anionic membrane and increases to 6.4 upon increasing anionic percentage to 75%.

Free simulations of multiple I-BAR dimers on the flat membrane surface

To identify possible oligomeric structures that might be responsible for generating or stabilizing tubular membranes, 2-20 I-BAR dimers were arranged on a rectangular lattice at a distance of 5 to 40 nm and were freely simulated on the flat membrane surface. In the simplest case, two dimers were freely simulated on a flat membrane in four independent runs. Most of the simulations resulted in lateral interactions. The lateral interactions can have various alignments, stabilized by salt bridges. This is expected due to the presence of an almost uniform distribution of the positively and negatively charged residues throughout the length of the dimer (Fig. S2). Lateral interactions (Fig. 2b and 2c) were more probable than end-to-end interactions (Fig. 2d). Aspartates 135, 166, 54, 181 and glutamates 7, 8, 174, 61, 65, 22, 140, 100, 91 and 238 contribute significantly to oligomerization. The end-to-end interactions are stabilized by hydrogen bonds involving residues LYS 152, ASN 153, SER151, GLY150 and GLN 155. However, the end-to-end interaction of just two dimers was not stable and eventually resulted in a laterally interacting dimer. In the next step, four dimers were freely simulated on the flat membrane surface. Within 1 ns, three dimers came together and formed a laterally overlapping higher oligomer as shown in Fig. 3. In further simulations of 6, 8, 9 and 20 dimers on a flat membrane both lateral and end-to-end interactions were encountered, but lateral interactions were more pronounced (e.g. Fig. S3 for 20 dimers). The oligomerization interface obtained from the free simulations on the flat membrane (Fig. 2b) is similar to that observed in the crystal structure (PDB id 1Y2O).

Free simulations of multiple I-BAR dimers were also carried out on the interior surface of a tubular membrane of 20-nm radius starting parallel or perpendicular to the tube axis. The dimers interacted with each other both laterally and end-to-end. Most of the dimers on the oligomeric form tended to orient parallel to the tube axis. Only a few dimers were stabilized in perpendicular orientation. Hence, our simulation shows increasing the protein concentration to ~544 dimers/μm^2 does not lead to a preference for perpendicular orientation relative to the tube axis.

Simulation of a chain and a sheet of dimers based on the crystal structure

Using the packing observed in the crystal structure we generated a chain of many dimers (Fig. 4a) and simulated it in implicit water as well as on a flat anionic membrane surface. The simulation in implicit water resulted in bending into a spiral shape with radius close to 20 nm within 10 ns (Fig. 4b). Importantly, the membrane binding interface lies on the convex surface of the spiral, indicating that the spiral would readily bind to a concave surface, as one would expect for a negative curvature generator. As mentioned earlier, the lateral interactions are not specific and can have various alignments. Regardless of the alignment, all constructed planar chains gave a spiral structure. On our flat implicit membrane surface, which is rigid and cannot deform, the simulation resulted in a 2-dimensional bent structure (Fig. 5).

Similarly, a planar I-BAR sheet was constructed containing both lateral and end-to-end interactions as shown in Fig. 6a and was simulated in implicit water. Within 5 ns, the sheet turns into a tubular structure as shown in Fig. 6b,c whose membrane binding interface is on the outside, suitable for fitting into the interior of an anionic tubular membrane. Interestingly, the sheet always bent along the direction of the lateral overlap of the dimers. This is another indication that the bent structure of the I-BAR oligomer arises from the lateral interactions. The obtained structure had a radius of ~13 nm, lower than the preferred curvature determined by experiment (29).

As a control, the sheet structure of two other I-BARs, MIM I-BAR (PDB ID 2D1L) and I-BARa (PDB ID 4NQI) were also simulated in the aqueous phase. Both I-BARs curved in such a way that the membrane binding surface lay on their convex surface. Interestingly, the curvature developed was smaller than that of IRSP53 I-BAR. This is consistent with the experimental finding that MIM I-BAR generates larger size tubules than IRSP53 I-BAR domain (29). Using the same protocol, an F-BAR sheet in aqueous solution (PDB ID 2V0O) developed a curvature with

the membrane binding interface on its concave surface, consistent with positive curvature generating behavior. The structures are shown in Fig. S4-S6.

Simulations of preformed spirals inside a tube

One of the important unresolved questions for I-BAR domains is how they arrange themselves inside membrane tubes. If they act like other BAR domains, they should also form helical oligomeric structures that stabilize the membrane tubules. It is very difficult to obtain such structures from free simulations of multiple BAR dimers in a reasonable time. An alternative approach is to simulate plausible preformed helical spirals. We designed two types of spirals, with lateral interaction and end-to-end interaction, taking into account the information from the free simulations. The helical spiral consisting of lateral interactions seems highly stable inside the cylindrical membrane tubes with 20 nm and 40 nm radii (Fig. 7 and S7). The pre-designed spiral with only end-to-end interactions appeared highly flexible and did not have a definite shape inside the membrane tube (Fig. S8). We also designed spirals with combination of lateral and end-to-end interactions where the two helical filaments with end-to-end interactions are laterally overlapping. To design such spirals, the octameric unit (Fig. S9) that was obtained from the free membrane simulations was replicated. The designed spirals with radii 20 nm and 40 nm (Fig. S10) appear rigid and entirely stable throughout the 20 ns simulations. In both, only the pitch of the helical structure changed to match its curvature preference. In the 40 nm tube the spiral continuously decreases its pitch indicating it prefers a higher curvature than the original. In this oligomeric structure, the orientational preference of individual dimers is satisfied, as they tend to remain parallel to the tube axis, especially inside the 20 nm tube.

In the next step, linear filaments were constructed with end-to-end interaction between the individual dimers as shown in Fig. S11. The filaments were then simulated on the flat membrane surface as well as on the interior of the membrane tube. In both simulations, the filaments failed to give a curved shape. This indicates that the end-to-end interaction alone is not sufficient for membrane bending. Based on these results we propose that the lateral interaction between the dimers is responsible for negative curvature generation and stabilization.

Binding energetics of low and high oligomers

Next, the curvature sensitivity of a dimer (Fig. 2c) and a tetramer (Fig. S9) of dimers was studied. The simulations were carried out on a 50% anionic interior tubular membrane. The binding energy (Table 4) is maximal at 10-20 nm and minimal at the flat membrane surface. The curvature sensitivity parameter α obtained from the 20 nm to 50 nm data is 4.0, almost four times that for a single dimer on the same membrane. This suggests that the dimer of dimers is more rigid and tends to have a curved shape. The tetrameric structure shown in Fig. S9 on a 20 nm tube was highly unstable and tended to fall apart at the end-to-end contacts. This supports the claim that end-to-end interactions do not support high curvature. However, this structure was stable on larger-size tubes with radius > 30 nm.

The binding energetics of the filaments (constructed with lateral interactions) on the flat membrane and the interior of cylindrical membranes with anionic fraction 50% are presented in Table S4 in supporting information. Binding energies as well as total energies are most favorable for the cylindrical spiral with radius 20 nm and least favorable for the filament on the flat membrane. This is consistent with the generation of smaller-size tubules. The sorting ratio between the flat and 20-nm cylindrical membrane, calculated from the average binding energy of the dimer with the membrane, is ~25.

Discussion

The main finding of this work is that oligomers of I-BAR domains attain a curvature that is unrelated, in fact nearly orthogonal, to the intrinsic curvature of the dimer along its principal axis. The curved oligomer exposes a convex membrane binding surface and is thus consistent with

generating negative membrane curvature. Both lateral and end-to-end interactions contribute to oligomerization, but the former are stronger. The relevant curvature develops along these lateral interactions, which can take place at various alignments. As a control, an F-BAR domain oligomer develops curvature in the opposite direction and is thus consistent with positive membrane curvature generation.

Experimental evidence on I-BAR oligomerization is scarce. Slow fluorescence recovery in the absence of stiffening of nanotubes coated with high density of ABBA I-BARs indicated possible oligomerization but with flexible linkages (43). Similar results were obtained with other BAR domains (44). It should be noted that no oligomerization of I-BAR domains has been observed in the aqueous phase (34). The fact that our oligomers are stable in water may be due to the short duration of the simulations or, more likely, to an overestimation of the driving forces for protein adhesion by the implicit solvent model. However, even if the stability of the oligomers is overestimated, the qualitative trends regarding curvature should be valid.

The radius of curvature that the IRSp53 I-BAR oligomer develops in our implicit water simulation is ~13 nm. This is smaller than the 20-nm tubules observed experimentally (29). One possible reason for this discrepancy is that the membrane deformation free energy increases as the tubule diameter decreases (45). Thus, the final tubule diameter is that which minimizes the free energy of the membrane+oligomer system. On the other hand, in pulled tube experiments, in which the membrane deformation free energy is already paid, optimal partitioning is observed for 18-nm tubes (34). Perhaps the presence of the membrane could influence the curvature of the oligomer. Of course, quantitative discrepancies could also be due to inaccuracies of our implicit water force field.

The pulled tube experiments (34) are so far the most detailed and quantitative. This and another study (43) found that the sorting ratio (partitioning coefficient) is higher at lower protein densities. This seems consistent with the formation of specific oligomeric structures in the tubule interiors which would correspond to an optimal protein density. As protein concentration increases, less optimal structures and curvatures are populated on the flat membrane and the sorting ratio decreases. The experiments showed the sorting ratio to be a function of the protein density. The sorting ratio was 20, 12 and 5 when the surface coverage on the pulled tubes was 20, 24 and 25%, respectively. Thus, the latter increases only slightly with protein concentration. The surface area coverage of our spiral on Fig. 7 is ~ 8.2%, about 3 times lower. The sorting ratio calculated from our binding free energies of the individual dimer is 1.8, 2.7 and 6.4 in 30%, 50% and 75% anionic membranes, respectively (Table S3). For the oligomeric forms the sorting ratio is substantially higher. For example, for the 20-dimer oligomeric spiral in 50% anionic membrane it is ~25 (Table S4). Precise determination of the sorting ratio requires detailed consideration of oligomerization equilibria and determination of accurate oligomeric structures on both the flat membrane and the tube.

Another important result of the pulled tube experiments is that the optimal radius of curvature is 18 nm (34). Our results reproduce the strengthened binding upon increasing the curvature to 20 nm and the reduction in binding from 20 nm to 10 nm at higher anionic fractions. At 30% anionic fraction, the binding affinity is about the same at 10 and 20 nm radius. We should note here the approximate nature of our binding affinity calculations. First, to calculate protein-membrane electrostatic interactions we use an approximate solution to the nonlinear Poisson-Boltzmann equation that is less accurate at high curvatures. Additionally, using the transfer energy as a proxy for the binding energy neglects possible deformation energy costs upon membrane binding. Protein configurational entropy effects are also neglected in our estimates.

Several studies suggested that the lipid PIP2 (PI(4,5)P2) plays a role in I-BAR function (29, 46). However, PIP2 is not strictly required for membrane remodeling (43, 47), suggesting no specific binding to BAR domains. At neutral pH PIP2 has a charge of -4 (48) and its clustering by I-BAR

(29) further increases the effective charge of the membrane and thus the binding energy. Our implicit membrane model neglects specific lipid binding effects and assumes uniform distribution of charge. Thus, to reproduce the behavior of a PIP2-containing membrane we need to use higher membrane anionic fractions than the nominal value. Considering this, the 50 or 70% anionic fractions where we observe the greatest curvature sensitivity are not unreasonable.

Previous MD simulations found that the IRSp53 domain flattens on the membrane and appears too flexible to support membrane remodeling based on its own intrinsic curvature (38). This is consistent with our results. Another all-atom simulation with a single I-BAR dimer could not generate the expected high negative curvature, implying that some some sort of oligomerization must play a role (37). Jarin et al. (39) used two levels of coarse-graining to study the aggregation behavior of I-BAR dimers on membranes of various geometries. They found that I-BAR aggregates oriented parallel to the tube axis when the tube radius was narrow (25 nm) and perpendicular when the tube was wider (radius 50 nm). This is in agreement with our results. Another highly coarse-grained model explored the effect of PIP2 clustering and found that preformed protrusion were stabilized by I-BAR dimers (40). Consistent with our results, they mainly observed two types of interactions; side-by-side and end-to-end, and these interactions were controlled by the strength of the membrane-protein interaction, protein curvature and the inclusion of the PIP2 patches on the membrane. However, these models employed purely repulsive protein-protein interactions and thus could not predict oligomers of definite shape.

The ultimate test of our mechanistic proposal would be to design mutations that would convert an I-BAR domain to an F-BAR domain. Given the multitude of interactions, this is challenging. Our approach could be extended to the study of other F-BAR and N-BAR peptides. Experimental techniques, such as EPR, that could measure distances between specific sites on the dimers could provide strict tests for our oligomer models.

Methods

IMM1_curv Model

Implicit membrane modeling was carried out with IMM1_curv (42), which can model spherical or cylindrical membranes of specified radius. IMM1 (49) is an implicit membrane model based on the effective energy function 1 (EEF1) (50). In EEF1, the solvation free energy is calculated as the sum of group contributions:

$$\Delta G^{slv} = \Sigma_i \Delta G_i^{slv} = \Sigma_i \Delta G_i^{ref} - \Sigma_i \Sigma_{j\neq i} f_i (r_{ij}) V_j \quad (1)$$

where ΔG_i^{slv} is the solvation free energy of atom i and ΔG_i^{ref} is the solvation free energy of atom i in a small model compound. The last term describes the loss of solvation due to surrounding groups; f_i is the solvation free energy density of atom I calculated as a Gaussian function of r_{ij}, r_{ij} is the distance between atoms i and j, and V_j is the volume of atom j.

In IMM1, ΔG_i^{ref} is modified to account for heterogenous membrane-water systems.

$$\Delta G^{ref}(z') = f(z') \Delta G_i^{ref,\ water} + (1 - f(z')) \Delta G_i^{ref;\ chex} \quad (2)$$

where $\Delta G_i^{ref,water}$ and $\Delta G_i^{ref;chex}$ are reference solvation free energies of atom i in water and cyclohexane, respectively. f(z´) is a sigmoidal function that describes the vertical transition from one phase to the other:

$$f(z') = z'^n/1 + z'^n, \qquad \text{where} \quad z' = |z|/(T/2) \quad (3)$$

where T is the thickness of the hydrophobic core of the membrane. The exponent n controls the steepness of the transition. The increase in electrostatic interactions inside a membrane is taken into account by a modified dielectric screening function given by,

$$\varepsilon = r^{f}_{ij}, \qquad f_{ij} = \alpha + (1-\alpha) \sqrt{f_i f_j} \quad (4)$$

where α is an empirical parameter and was adjusted to 0.85 which gives membrane binding energies close to experiment.

IMM1-curv modifies the shape of the hydrophobic region to account for a cylindrical or spherical shape. The center of the sphere is placed at the origin and R is the distance between the origin and the sphere mid-surface. The equation for z above is modified to z´ = |r-R|/(T/2) where r is the distance of the atom from the origin, given by

$$r = \sqrt{x^2 + y^2 + z^2} \quad (5)$$

For a cylinder the x component is omitted, assuming that the cylindrical axis is along the x axis. The lateral pressure profile further takes account the lipid packing effect as a result of the curvature. Approximate Poisson-Boltzmann equations were used to calculate the electrostatic interaction between the protein and anionic membrane with spherical and cylindrical shapes.

Computational Details

The MD simulations were carried out with the CHARMM package version c44a2 (51). The simulations were run for 20-ns at 300 K with a 2-fs time step. The trajectories were saved every 1 ps and analysis was done on the last 10 ns. The initial structure of the dimer was obtained from PDB code 1Y2O (52). In the IMM1 calculations, the width of the membrane hydrophobic core was set to 25.4 Å and the anionic fraction was set to 30%. For the higher oligomers, 50% anionic membrane was used. The charge layer was set 3 Å outward from the hydrophobic-hydrophilic interface and 0.1 M salt concentration was used. Since membrane binding is dominated by electrostatic interactions, calculations were carried out without the lateral pressure component. Multiple trials were averaged to estimate statistical uncertainty. The binding energies were estimated as average transfer energies, i.e. the difference in energy of the peptides on the membrane surface and the same conformation in bulk water.

A quantitative measure of curvature sensitivity was done by calculating the parameter α defined by the equation below (42).

$$\Delta G^{o} = \text{constant} + \alpha \times RT \times \ln r \quad (6)$$

where r is the radius of the curvature.

Acknowledgments

This work was supported by the NIH (GM117146) and the NSF (MCB 1855942). Infrastructure support was provided in part by Research Centers in Minority Institutions grant no. 8G12MD007603 from the NIH.

References

1. M. Kaksonen, A. Roux, Mechanisms of clathrin-mediated endocytosis. *Nature Reviews Molecular Cell Biology* **19**, 313 (2018).
2. G. Eitzen, Actin remodeling to facilitate membrane fusion. *Biochimica et Biophysica Acta (BBA) - Molecular Cell Research* **1641**, 175-181 (2003).
3. P. Chlanda *et al.*, Palmitoylation Contributes to Membrane Curvature in Influenza A Virus Assembly and Hemagglutinin-Mediated Membrane Fusion. *Journal of Virology* **91** (2017).
4. J. M. Besterman, R. B. Low, Endocytosis: a review of mechanisms and plasma membrane dynamics. *Biochemical Journal* **210**, 1-13 (1983).
5. Y. A. Chen, R. H. Scheller, SNARE-mediated membrane fusion. *Nature Reviews Molecular Cell Biology* **2**, 98 (2001).

6. L.-G. Wu, E. Hamid, W. Shin, H.-C. Chiang, Exocytosis and Endocytosis: Modes, Functions, and Coupling Mechanisms. *Annual Review of Physiology* **76**, 301-331 (2014).
7. L. V. Chernomordik, M. M. Kozlov, Mechanics of membrane fusion. *Nature Structural &Amp; Molecular Biology* **15**, 675 (2008).
8. S. Suetsugu, The proposed functions of membrane curvatures mediated by the BAR domain superfamily proteins. *The Journal of Biochemistry* **148**, 1-12 (2010).
9. M. M. Kozlov *et al.*, Mechanisms shaping cell membranes. *Current Opinion in Cell Biology* **29**, 53-60 (2014).
10. H. T. McMahon, J. L. Gallop, Membrane curvature and mechanisms of dynamic cell membrane remodelling. *Nature* **438**, 590 (2005).
11. T. Baumgart, B. R. Capraro, C. Zhu, S. L. Das, Thermodynamics and Mechanics of Membrane Curvature Generation and Sensing by Proteins and Lipids. *Annu. Rev. Phys. Chem.* **62**, 483-506 (2011).
12. F. Campelo, H. T. McMahon, M. M. Kozlov, The Hydrophobic Insertion Mechanism of Membrane Curvature Generation by Proteins. *Biophysical Journal* **95**, 2325-2339 (2008).
13. J. Zimmerberg, M. M. Kozlov, How proteins produce cellular membrane curvature. *Nature Reviews Molecular Cell Biology* **7**, 9 (2005).
14. G. Drin, B. Antonny, Amphipathic helices and membrane curvature. *FEBS Letters* **584**, 1840-1847 (2010).
15. C. Mim, V. M. Unger, Membrane curvature and its generation by BAR proteins. *Trends in Biochemical Sciences* **37**, 526-533 (2012).
16. C. Mim *et al.*, Structural Basis of Membrane Bending by the N-BAR Protein Endophilin. *Cell* **149**, 137-145 (2012).
17. S. Suetsugu, K. Toyooka, Y. Senju, Subcellular membrane curvature mediated by the BAR domain superfamily proteins. *Seminars in Cell & Developmental Biology* **21**, 340-349 (2010).
18. M. Simunovic, G. A. Voth, A. Callan-Jones, P. Bassereau, When Physics Takes Over: BAR Proteins and Membrane Curvature. *Trends in Cell Biology* **25**, 780-792 (2015).
19. J. C. Stachowiak *et al.*, Membrane bending by protein–protein crowding. *Nature Cell Biology* **14**, 944 (2012).
20. R. N. Frese *et al.*, Protein Shape and Crowding Drive Domain Formation and Curvature in Biological Membranes. *Biophysical Journal* **94**, 640-647 (2008).
21. J. Derganc, B. Antonny, A. Čopič, Membrane bending: the power of protein imbalance. *Trends in Biochemical Sciences* **38**, 576-584 (2013).
22. T. Kirchhausen, Bending membranes. *Nature Cell Biology* **14**, 906 (2012).
23. J. Derganc, A. Čopič, Membrane bending by protein crowding is affected by protein lateral confinement. *Biochimica et Biophysica Acta (BBA) - Biomembranes* **1858**, 1152-1159 (2016).
24. M. Masuda *et al.*, Endophilin BAR domain drives membrane curvature by two newly identified structure-based mechanisms. *The EMBO Journal* **25**, 2889-2897 (2006).
25. B. J. Peter *et al.*, BAR Domains as Sensors of Membrane Curvature: The Amphiphysin BAR Structure. *Science* **303**, 495-499 (2004).
26. X. Pang *et al.*, A PH Domain in ACAP1 Possesses Key Features of the BAR Domain in Promoting Membrane Curvature. *Developmental Cell* **31**, 73-86 (2014).
27. G. Zhu *et al.*, Structure of the APPL1 BAR-PH domain and characterization of its interaction with Rab5. *The EMBO Journal* **26**, 3484-3493 (2007).

28. A. Frost *et al.*, Structural Basis of Membrane Invagination by F-BAR Domains. *Cell* **132**, 807-817 (2008).
29. J. Saarikangas *et al.*, Molecular Mechanisms of Membrane Deformation by I-BAR Domain Proteins. *Current Biology* **19**, 95-107 (2009).
30. J. Linkner *et al.*, The inverse BAR domain protein IBARa drives membrane remodeling to control osmoregulation, phagocytosis and cytokinesis. *Journal of Cell Science* **127**, 1279-1292 (2014).
31. J. Saarikangas, H. Zhao, P. Lappalainen, Regulation of the Actin Cytoskeleton-Plasma Membrane Interplay by Phosphoinositides. *Physiological Reviews* **90**, 259-289 (2010).
32. S. Shukla, R. Jin, J. Robustelli, Z. E. Zimmerman, T. Baumgart, PIP2 Reshapes Membranes through Asymmetric Desorption. *Biophysical Journal* **117**, 962-974 (2019).
33. Z. T. Graber, Z. Shi, T. Baumgart, Cations induce shape remodeling of negatively charged phospholipid membranes. *Physical Chemistry Chemical Physics* **19**, 15285-15295 (2017).
34. C. Prévost *et al.*, IRSp53 senses negative membrane curvature and phase separates along membrane tubules. *Nature Communications* **6**, 8529 (2015).
35. G. Emilsson *et al.*, Nanoplasmonic Sensor Detects Preferential Binding of IRSp53 to Negative Membrane Curvature. http://dx.doi.org/10.3389/fchem.2019.00001.
36. A. Breuer, L. Lauritsen, E. Bertseva, I. Vonkova, D. Stamou, Quantitative investigation of negative membrane curvature sensing and generation by I-BARs in filopodia of living cells. *Soft Matter* **15**, 9829-9839 (2019).
37. O. V. Levtsova, I. D. Davletov, O. S. Sokolova, K. V. Shaitan, A molecular dynamics study of the interaction between domain I-BAR of the IRSp53 protein and negatively charged membranes. *Biophysics* **56**, 220-224 (2011).
38. K. Takemura, K. Hanawa-Suetsugu, S. Suetsugu, A. Kitao, Salt Bridge Formation between the I-BAR Domain and Lipids Increases Lipid Density and Membrane Curvature. *Scientific Reports* **7**, 6808 (2017).
39. Z. Jarin *et al.*, Unusual Organization of I-BAR Proteins on Tubular and Vesicular Membranes. *Biophysical Journal* **117**, 553-562 (2019).
40. Z. Jarin, A. J. Pak, P. Bassereau, G. A. Voth, Membrane-mediated forces can stabilize tubular assemblies of I-Bar proteins. *bioRxiv* 10.1101/2020.06.10.144527, 2020.2006.2010.144527 (2020).
41. X. Lin *et al.*, Roles of PIP2 in the membrane binding of MIM I-BAR: insights from molecular dynamics simulations. *FEBS Letters* **592**, 2533-2542 (2018).
42. B. Nepal, J. Leveritt, T. Lazaridis, Membrane Curvature Sensing by Amphipathic Helices: Insights from Implicit Membrane Modeling. *Biophysical Journal* **114**, 2128-2141 (2018).
43. Y. F. Barooji, A. Rørvig-Lund, S. Semsey, S. N. S. Reihani, P. M. Bendix, Dynamics of membrane nanotubes coated with I-BAR. *Scientific Reports* **6**, 30054 (2016).
44. H. Zhao *et al.*, Membrane-sculpting BAR domains generate stable lipid microdomains. *Cell Reports* **4**, 1213-1223 (2013).
45. Alexander J. Sodt, Richard W. Pastor, Molecular Modeling of Lipid Membrane Curvature Induction by a Peptide: More than Simply Shape. *Biophysical Journal* **106**, 1958-1969 (2014).
46. P. K. Mattila *et al.*, Missing-in-metastasis and IRSp53 deform PI(4,5)P2-rich membranes by an inverse BAR domain–like mechanism. *Journal of Cell Biology* **176**, 953-964 (2007).
47. Z. Chen, Z. Shi, T. Baumgart, Regulation of Membrane-Shape Transitions Induced by I-BAR Domains. *Biophysical Journal* **109**, 298-307 (2015).

48. D. A. Brown, PIP2Clustering: From model membranes to cells. *Chemistry and Physics of Lipids* **192**, 33-40 (2015).
49. T. Lazaridis, Effective energy function for proteins in lipid membranes. *Proteins: Structure, Function, and Bioinformatics* **52**, 176-192 (2003).
50. T. Lazaridis, M. Karplus, Effective energy function for proteins in solution. *Proteins: Structure, Function, and Bioinformatics* **35**, 133-152 (1999).
51. B. R. Brooks *et al.*, CHARMM: The biomolecular simulation program. *Journal of Computational Chemistry* **30**, 1545-1614 (2009).
52. T. H. Millard *et al.*, Structural basis of filopodia formation induced by the IRSp53/MIM homology domain of human IRSp53. *The EMBO Journal* **24**, 240-250 (2005).

Figures and Tables

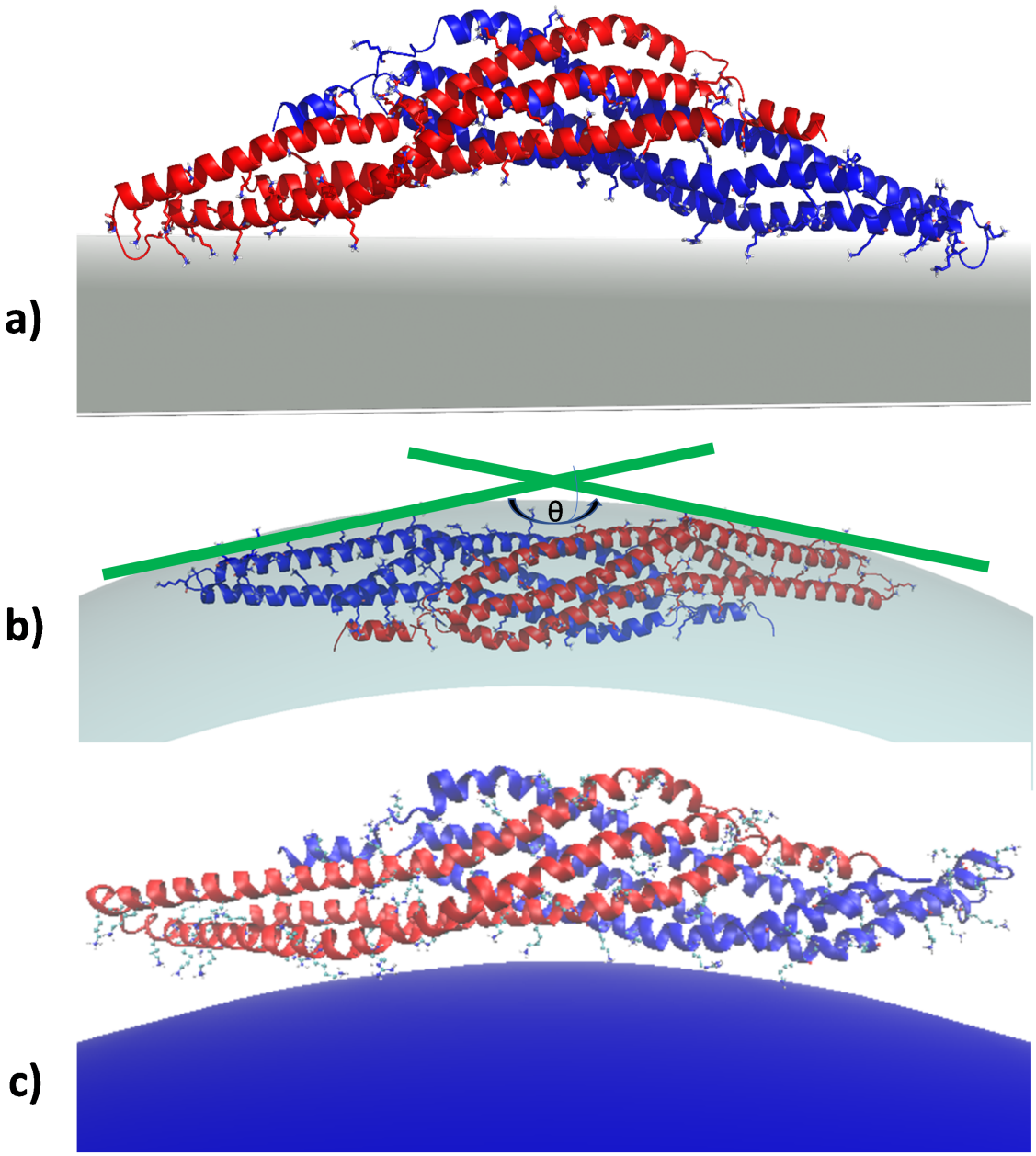

Figure 1. The binding configuration of the dimer on the flat membrane surface (a), on an interior spherical surface of radius 30 nm (b), and on an exterior spherical surface of radius 30 nm (c), after 20 ns simulation. The positively charged residues are shown in stick model.

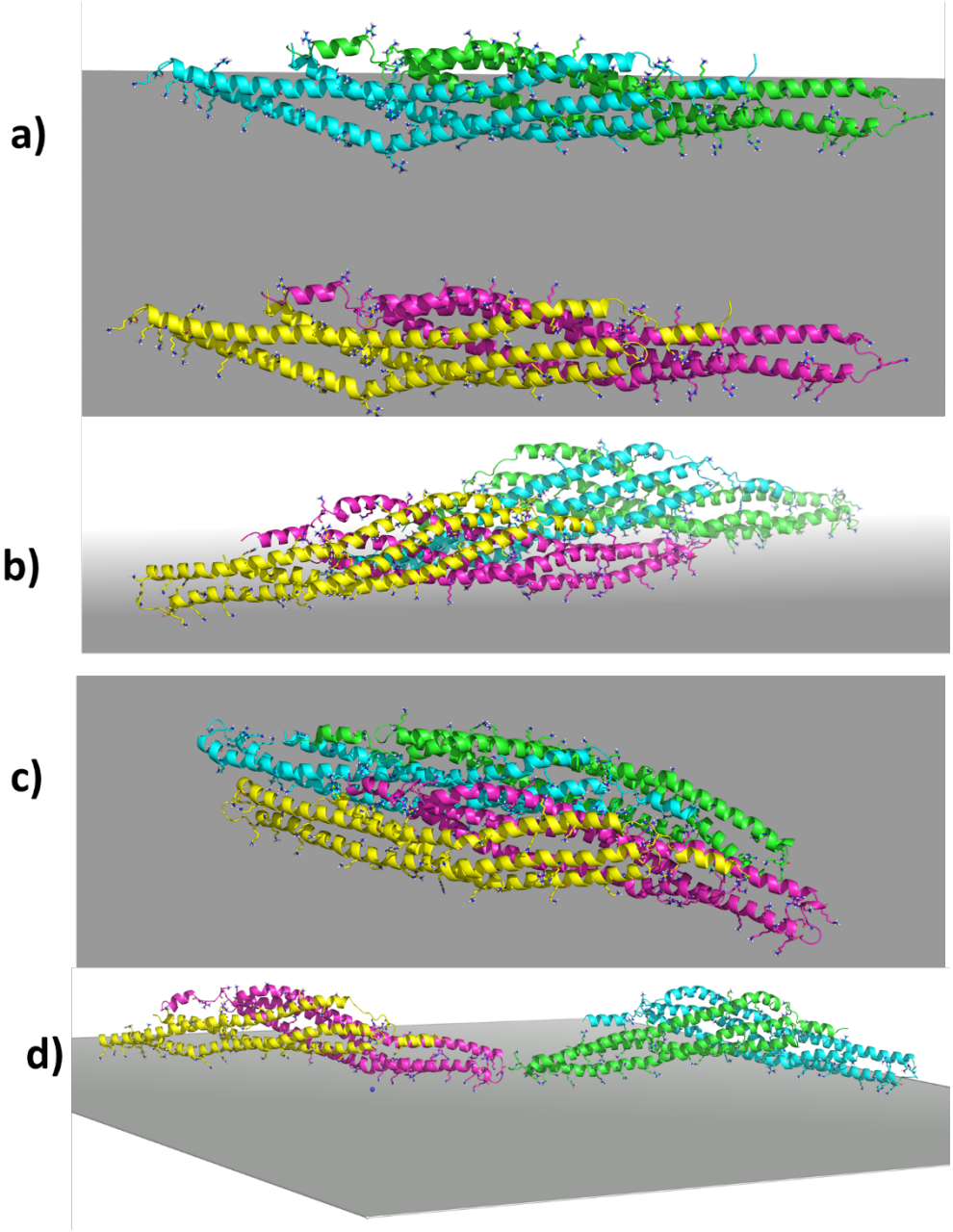

Figure 2. Final configurations of the 20 ns free simulations of two bar dimers on the flat membrane surface: a) initial configuration, b), c) and d) are final configurations in different trials.

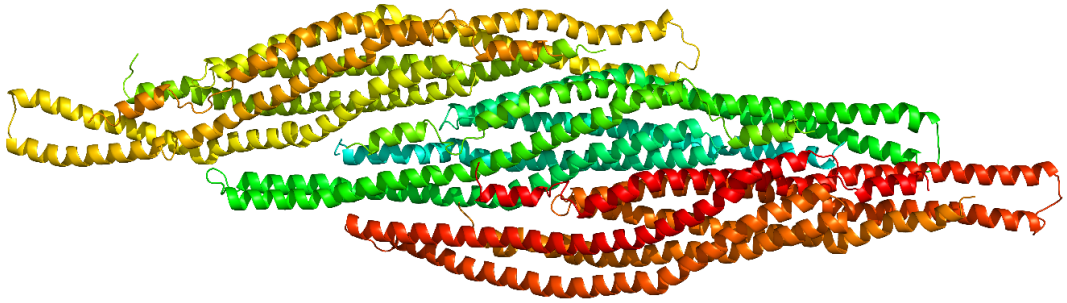

Figure 3. Trimeric oligomer obtained from the free simulation of four dimers on the flat membrane surface

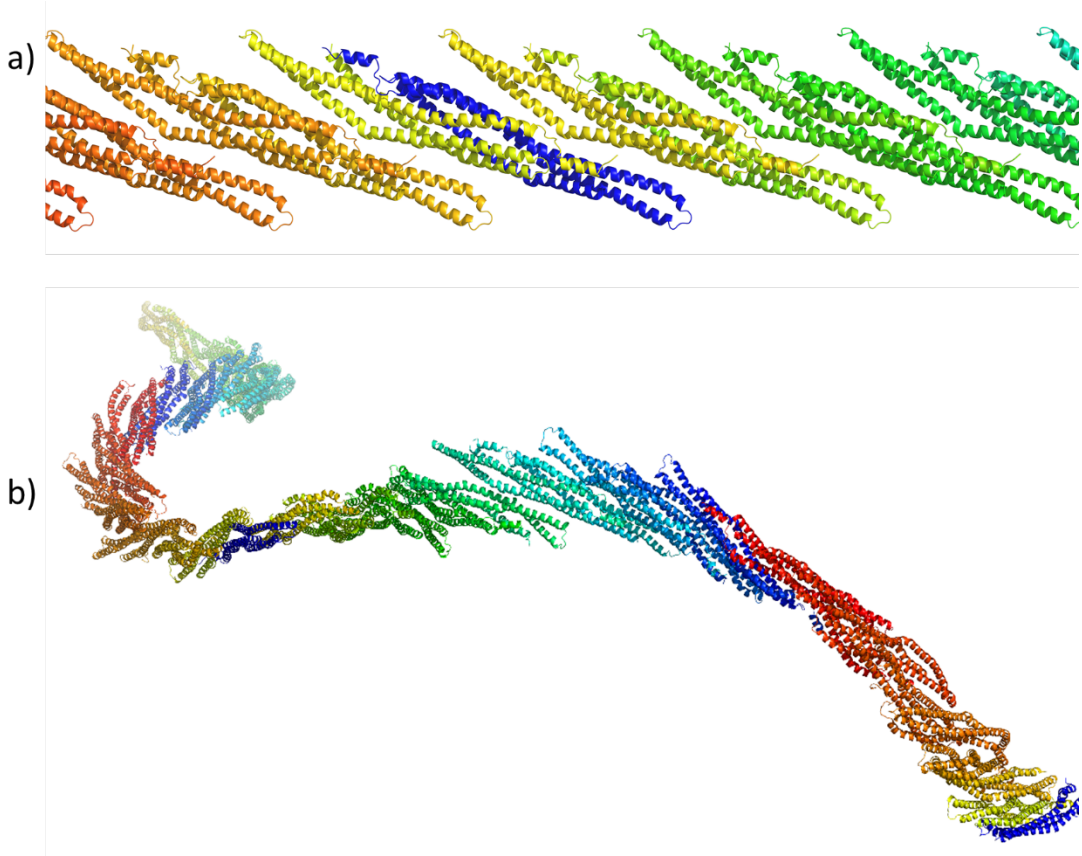

Figure 4. a) Initial arrangement of the dimers in the crystal structure, (b) final conformation obtained after 20 ns simulation in implicit water

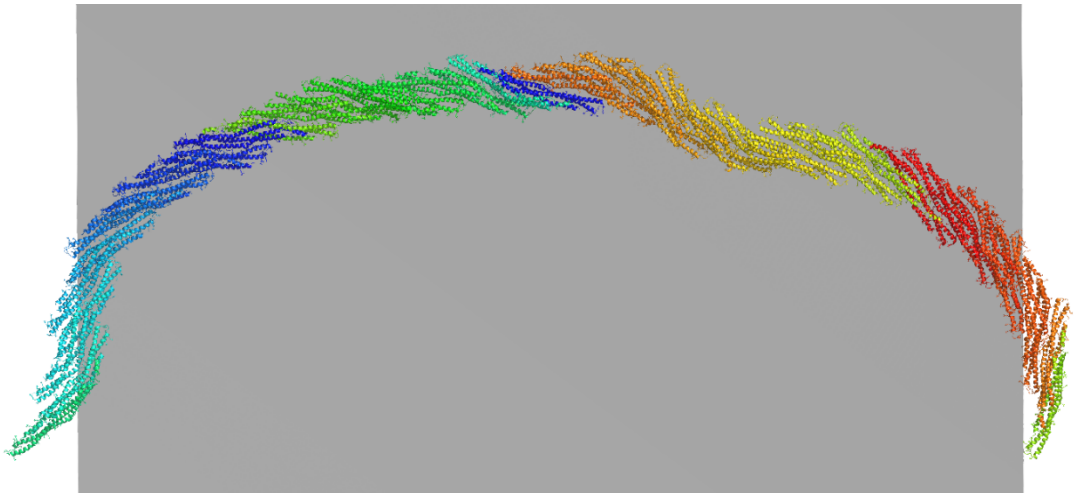

Figure 5. Curved conformation obtained from the simulation of the planar chain of dimers based on the crystal structure on a flat membrane surface

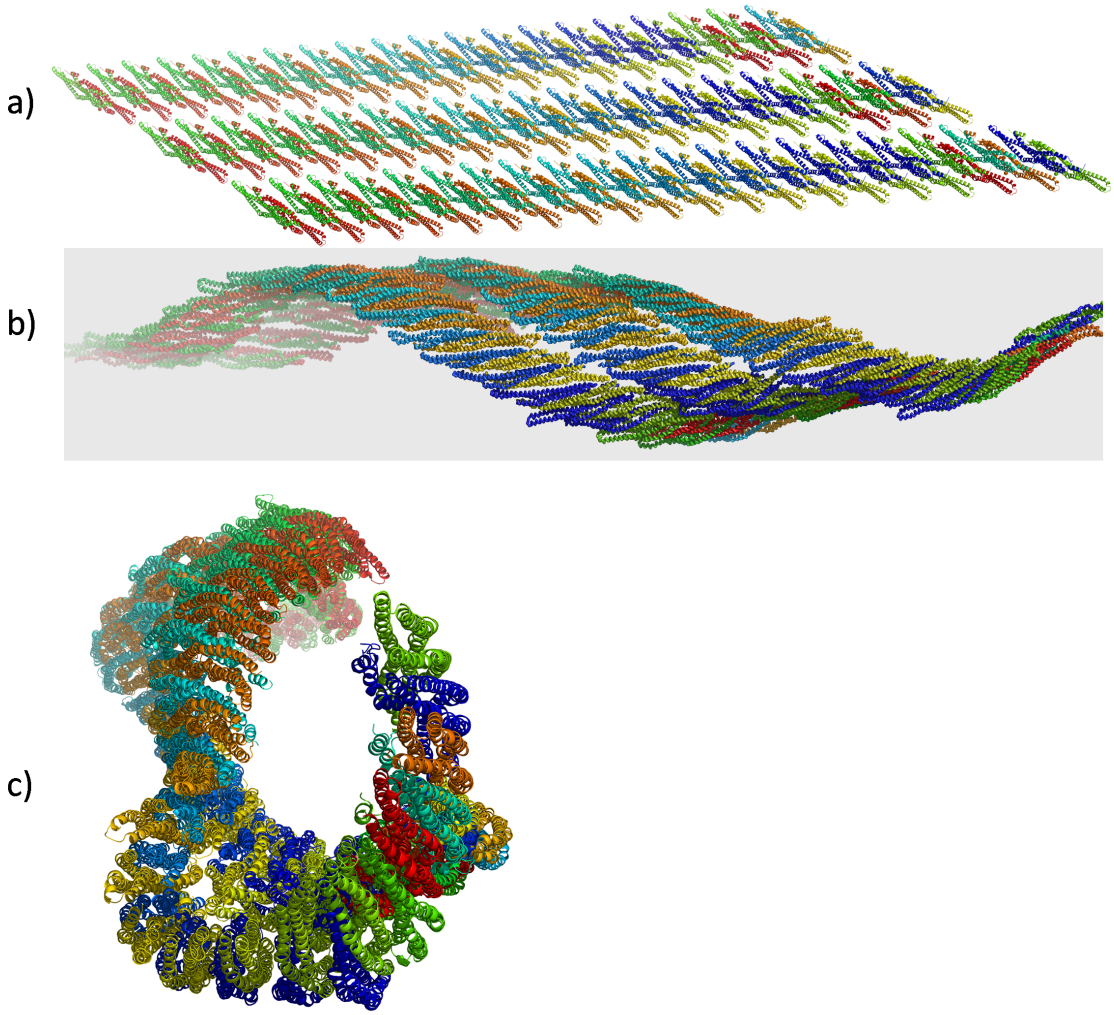

Figure 6. Initial structure of the planar I-BAR dimer sheet (a) and final structure after simulation in implicit water (b), side view and c) view along cylindrical axis.

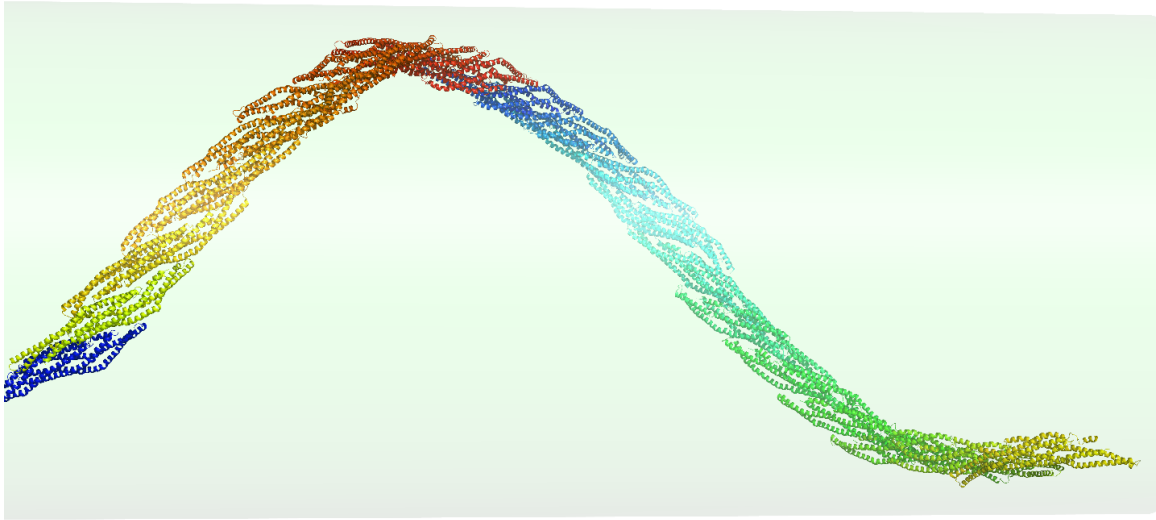

Figure 7. Final configuration of the pre-designed spiral after 20 ns simulation in the interior of a 20-nm cylindrical tube

Table 1. Tilt angle of I-BAR dimer with respect to the tube axis. Initially, the protein was placed parallel to the tube axis except one trial which was started in a perpendicular orientation.

	20nm	30nm	40nm	50nm
Inside				
Trial 1	12±3	19±3	85±9	3±5
Trial 2	8±4	29±2	6±2	90±3
Trial 3	6±3	17±2	23±2	84±2
Trial 4	17±3	3±2	29±2	7±3
Perpendicular	16±9	30±3	88±3	85±6
outside				
Trial 1	12±2	10±2	10±4	13±2
Trial 2	6±2	14±1	21±3	13±2
Trial 3	13±2	1±2	2±2	10±2
Perpendicular	20±3	28±2	15±3	12±3

Table 2. Binding energies of I-BAR dimer on cylindrical and spherical lipid membranes with 30% anionic fraction.

sphere						flat
	10nm	20nm	30nm	40nm	50nm	
Inside	-[a]	-7.2±0.3	-7.3±0.3	-7.2±0.2	-7.6±0.3	-7.3±0.5
Outside	-4.8±0.4	-5.5±0.5	-6.4±0.5	-7.2±0.5	-6.8±0.6	
cylinder						
	10nm	20nm	30nm	40nm	50nm	
Inside	-7.6±0.1	-7.6±0.4	-7.4±0.4	-7.3±0.5	-7.4±0.1	
Outside	-6.8±0.3	-7.3±0.3	-7.5±0.1	-7.2±0.2	-7.1±0.6	

a. The dimer is too long to fit inside a 10-nm sphere.

Table 3. Binding energies of I-BAR dimer on cylindrical membrane of different anionic fractions

Anionic Fraction	10nm	20nm	30nm	40nm	50nm	flat	α
30%	-7.6±0.1	-7.6±0.4	-7.4±0.4	-7.3±0.5	-7.4±0.1	-7.3±0.5	0.4±0.2
50%	-11.0±0.1	-11.2±0.4	-11.2±0.4	-10.8±0.1	-10.6±0.9	-10.6±0.1	1.2±0.4
75%	-13.6±0.1	-14.1±0.5	-14.0±0.2	-13.6±0.4	-13.5±0.3	-13.0±0.5	1.3±0.2

Table 4. Binding and total energy of a dimer of dimers of i-bar on a 50% anionic membrane. Averages were calculated from three trials and the last 10 ns of a 20-ns simulation.

Radius, nm	10nm	20nm	30nm	40nm	50nm	Flat	α
Binding energy	-20.6±0.3	-20.5±0.5	-19.5±0.6	-18.9±0.3	-18.3±0.9	-18.0±0.6	4.0±0.1
Total Energy	-24169±3	-24159±3	-24153±19	-24154±6	-24150±11	-24145±15	